The Supersonic Mode and the Role of Wall Temperature in Hypersonic Boundary Layers with Thermochemical Nonequilibrium Effects

Carleton P. Knisely* and Xiaolin Zhong†

University of California, Los Angeles, California, 90095, USA

There has been a renewed interest in studying the stability of the supersonic mode in hypersonic boundary layers. The supersonic mode, sometimes also referred to as the spontaneous radiation of sound, is associated with an unstable Mack's second mode synchronizing with the slow acoustic spectrum, causing the disturbance to travel upstream supersonically relative to the meanflow outside the boundary layer. Recent theoretical results have shown the possibility of the supersonic mode existing in hot-wall flows, which is contrary to decades of research on the supersonic mode suggesting it is an artifact of hypersonic cold-wall ($T_w/T_\infty < 1$) flows. The flow conditions leading to the supersonic mode have not been thoroughly and systematically investigated. As a result, it is unknown whether or not the supersonic mode can become the dominant boundary layer instability over the traditional second mode. This work uses thermochemical nonequilibrium Direct Numerical Simulation (DNS) along with thermochemical nonequilibrium Linear Stability Theory (LST) to replicate the flow conditions used in the theoretical study to obtain a more complete investigation of the supersonic mode in both hot-wall and cold-wall flow conditions. The purpose is to analyze the effect of wall temperature on the supersonic mode at high-enthalpy conditions. The simulation is Mach 10 flow over a 1mm nose radius axisymmetric cone 1 meter in length. LST results indicate that the supersonic mode does not exist in neither the hot-wall nor the cold-wall flows, however unsteady DNS results indicate the presence of the spontaneous radiation of sound in both cases, going against LST predictions. Further FFT analysis indicated that this sound radiation was an artifact of the interaction between an unstable subsonic mode S, stable supersonic mode F1, and the slow acoustic spectrum. The supersonic mode found in the cold-wall case had a significantly higher magnitude than the hot-wall case, demonstrating that a colder wall produces a stronger supersonic mode. Additionally, the magnitude of the supersonic mode in the cold-wall case was higher than the magnitude of the traditional second mode and could impact transition unexpectedly if not accounted for.

I. Introduction

It has long been known that boundary layer transition from laminar to turbulent has a considerable impact on the design of hypersonic vehicles.[1–3] Transition to turbulent flow drastically increases drag and heating to the vehicle surface, and can have a prominent effect on control of the hypersonic vehicle. It also affects engine performance and operability as well as vehicle structure and weight. The heating to the vehicle surface is one of the primary considerations in hypersonic vehicle design. Thermal protection systems (TPSs) are required to prevent the surface of the vehicle from overheating and failing. TPSs are usually specified with a large factor of safety to ensure protection of the vehicle, although this often adds unnecessary weight, reducing the maximum payload. The ability to predict accurately or even to delay the onset of transition and maintain laminar flow can have a significant payoff in terms of the reduction in aerodynamic heating, higher fuel efficiency, and weight of the thermal protection system.

*Graduate Student, Mechanical and Aerospace Engineering, carleton.knisely@gmail.com, AIAA Student Member.

†Professor, Mechanical and Aerospace Engineering, xiaolin@seas.ucla.edu, AIAA Associate Fellow.

Mack[4] found that the major instability waves leading to transition to turbulence in a perfect gas flow are the first and second modes, which Fedorov[3] recently described as acoustic rays physically trapped between the wall and sonic line. A schematic for the second mode similar to Fedorov's is shown in Fig. 1. First, however, it is important to define Fedorov's sonic line and the rationale for this physical description. A useful parameter describing the speed of propagation of the disturbance relative to the mean flow is the local relative Mach number

$$M_r(y) = \frac{\overline{u}(y) - c_r}{\overline{a}(y)} \tag{1}$$

where $\overline{u}(y)$ is the local mean flow velocity tangential to the wall, $c_r = \omega/\sqrt{\beta_r^2 + \alpha_r^2}$ is the disturbance propagation speed with ω the circular frequency, β_r the spanwise wavenumber, and α_r the real component of the streamwise wave number, and $\overline{a}(y)$ is the local mean flow speed of sound. The local relative Mach number appears in the nondimensional temporal stability equations, as presented by Mack[5] as $\overline{M}$ in his Eq. (9.16)[a]:

$$D\left[\hat{v}/(\tilde{\alpha}\tilde{U} - \omega)\right] - \tilde{\alpha}^2(1 - \overline{M}^2)\left[\hat{v}/(\tilde{\alpha}\tilde{U} - \omega)\right] = 0 \tag{2}$$

where $D = d/dy$, $\hat{v}$ is the wall-normal velocity complex eigenfunction, $\tilde{\alpha}\tilde{U} = \alpha U + \beta W$, where α and β are the streamwise and spanwise complex wavenumbers, respectively, and U and W are the streamwise and spanwise mean flow velocities, respectively, $\tilde{\alpha}^2 = \alpha^2 + \beta^2$, and ω is the complex frequency. From Eq. 2, it is clear that the governing stability equation changes its character from an elliptic differential equation to a hyperbolic equation as $|M_r|$ increases past unity ($\overline{M}$ in Mack's notation). This change in character is responsible for different behavior of the boundary layer depending on the value of M_r.

The relative sonic line described by Fedorov[3] is then given by $M_r(y) = -1$, or $c_r = \overline{u}(y) + \overline{a}(y)$ in Fig. 1. Near the wall, the disturbance is propagating downstream supersonically ($M_r < -1$) with respect to the local mean flow velocity. In this region where $M_r < -1$, the stability equations are hyperbolic, resulting in the acoustic disturbance waves trapped by the wall with the relative sonic line acting as a wave guide.[3] Outside of $M_r = -1$, the disturbance is traveling subsonically with respect to the free stream, and creates a "rope-like" wave pattern observed by many researchers both experimentally[6,7] and numerically.[8–10] These structures are centered about $M_r = 0$, or equivalently $c_r = \overline{u}(y)$.

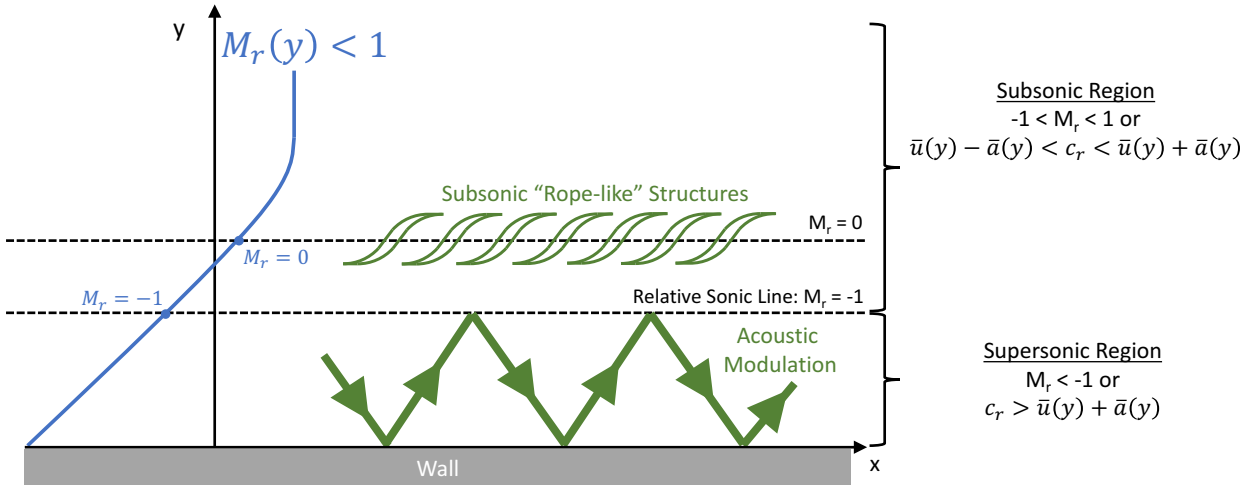

Figure 1. Schematic of Mack's second mode similar to Fedorov's.[3]

Researchers have developed numerical tools to predict transition to turbulence due to the first and second mode. Malik[11] implemented multiple numerical methods for solving the Linear Stability Theory (LST) equations for a perfect gas. Chemical nonequilibrium effects in the LST framework were studied numerically by Stuckert and Reed.[12] Hudson et al.[13] incorporated thermal nonequilibrium effects in addition to chemical nonequilibrium for LST. Johnson et al.[14–16] studied hypersonic boundary layer transition in thermochemical nonequilibrium using the Parabolized Stability Equations (PSE), which account for nonparallel flow effects

[a]simplified version of the stability equation assuming large $\tilde{\alpha}^2$

that are ignored in LST. Overall, the researchers determined that dissociation of air species is stabilizing to the first mode, but destabilizing to the second mode. Additionally, it was determined that thermal nonequilibrium has a slight destabilizing effect on the first mode, and a slight stabilizing effect on the second mode.

When the traditional mode S is the unstable second mode, its phase speed is subsonic, i.e. $1 - 1/M_\infty < c_r < 1 + 1/M_\infty$. Although most hypersonic boundary layer transition studies have primarily focused on the second mode in which mode S is unstable, it has been shown that when mode F1 is unstable, there can be an interaction between mode F1 and the slow acoustic spectrum downstream of the mode F1/S synchronization location.[17,18] That is, the unstable second mode (F1) can synchronize with the slow acoustic spectrum, causing an energy exchange. Downstream of this synchronization with the slow acoustic spectrum, the unstable mode F1 has a supersonic phase speed, i.e. $c_r < 1 - 1/M_\infty$. When this situation occurs, the unstable mode F1 is referred to as the supersonic mode, and it is associated with unique features not present in traditional flows with a subsonic second mode. In particular, the supersonic modes cause second-mode instabilities over a wider range of frequencies than subsonic modes and cause acoustic waves to radiate from the wall into the free stream.

A schematic of the supersonic mode developed by Knisely and Zhong[19] is presented in Fig. 2 for further elaboration. Near the wall, the same structures exist as in the traditional second mode. The disturbance is traveling supersonically downstream relative to the mean flow, indicated below a relative Mach number of $M_r < -1$, or equivalently $c_r > \overline{u}(y) + \overline{a}(y)$. The sonic line $M_r = -1$ again acts as a wave guide for the acoustic rays.[3] Similar to the traditional second mode, outside of $M_r = -1$, the disturbance is traveling subsonically with respect to the free stream, and creates the "rope-like" wave pattern. In some flows under very particular flow conditions, a second supersonic region can be present. There can exist a second relative sonic line $M_r = 1$, or equivalently $c_r < \overline{u}(y) - \overline{a}(y)$, outside of which the disturbance is traveling *upstream* supersonically with respect to the free stream. Again, because $|M_r| > 1$, the stability equations are hyperbolic and the solution is wave-like. This creates the "slanted" wave pattern outside of the boundary layer shown in the schematic in Fig. 2. The angle created by this decaying wave pattern is analogous to a Mach wave angle from traditional compressible flow theory, and is given by $\mu = \arcsin(1/M_r)$.

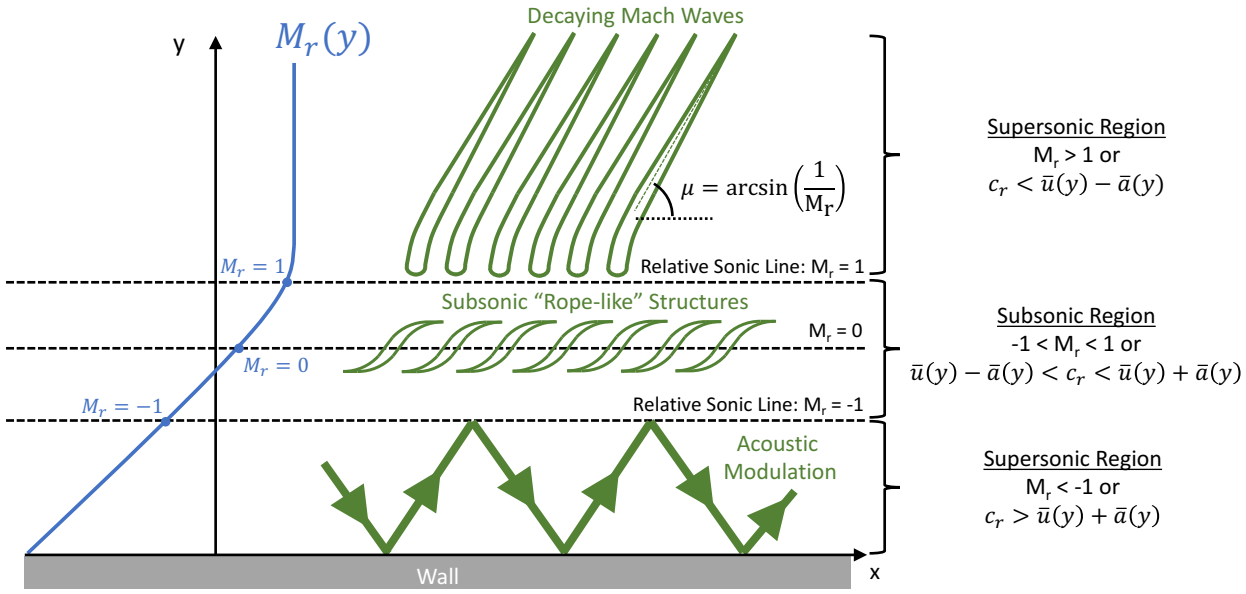

Figure 2. Schematic of supersonic mode.

Although early studies by Mack in 1985[17] and 1990[18] and Reshotko in 1991[1] came to the consensus that the supersonic mode was insignificant due to its smaller disturbance amplification rate than the second mode, there has been a renewed interest in studying the supersonic mode in hypersonic boundary layers due to their presence in the flow conditions typical of the T5 shock tunnel at Caltech. In such high-enthalpy shock tube experiments, the wall temperature remains ambient during the short test duration, resulting in a cold wall with respect to the free stream. Cold wall conditions in high-enthalpy flows are also found in some

real flight cases.[20,21] It has long been known through studies by Lees[22] and Mack[17,23] that wall cooling stabilizes the first mode but destabilizes the second mode. Bitter and Shepherd[24] in 2015 took these studies a few steps further and have shown through a chemical equilibrium, thermal nonequilibrium LST analysis that high levels of wall cooling on a flat plate lead to unique features, in particular an unstable second mode traveling upstream supersonically relative to the free stream. The supersonic modes cause instabilities over a wider range of frequencies than subsonic modes and cause acoustic waves to radiate from the wall into the free stream. This phenomenon has also been referred to as the spontaneous radiation of sound by Fedorov.[25]

Despite the existence of the supersonic mode being known since the mid 1980's by Mack[17,18] and Reshotko in the early 1990's,[1] a comprehensive examination of its impact on transition to turbulence is yet to be performed. There have been only a few studies in which the supersonic mode's characteristics were the direct focus of the investigation. In 1997 Chang, Vinh, and Malik[26] reported supersonic modes in Mach 20 chemical nonequilibrium, thermal equilibrium flow over a 6 degree wedge with wall temperature ratio $T_w/T_{ad} = 0.1$, and noted the stability boundary conditions in the free stream are critical to resolving the supersonic mode due to its oscillatory nature in the free stream. Additionally, they note that peak species perturbation coincides with the location of maximum chemical production in the boundary layer, and therefore the species eigenfunctions do not oscillate in the free stream, whereas pressure, temperature, and velocity perturbations exhibit the oscillatory behavior outside of the boundary layer. Over a decade later came a resurgence of the supersonic mode, however in most cases it was not the primary focus of the study. In 2011 Fedorov *et al.*[27] encountered unstable supersonic modes in flow with resonating micro-cavities on a flat plate. Wagnild[28] observed the spontaneous radiation of sound in 2012 on a 5-degree half-angle sharp cone, although the focus of his study was the effect of vibrational nonequilibrium on boundary layer stability. In 2013 Bres *et al.*[29] also found this phenomenon in flow over a wall with a porous coating on a flat plate. Klentzman and Tumin[30] in 2013 also commented on the supersonic mode in a cold-wall flat plate flow using oxygen. Jewell[31] in 2014 performed numerical calculations to supplement experimental results from the T5 tunnel at Caltech. Jewell's numerical results showed the supersonic mode on a 5-degree half-angle sharp cone, although the focus of his dissertation was transition delay with CO_2 concentration, turbulent spot propagation, and transition control via gas injection. In the same year, Fedorov, Soudakov, and Leyva[32] found unstable supersonic modes on a 5-degree half-angle cone with gas injection. Over the course of 2014-2016, Salemi *et al.* also modeled the 5-degree half-angle sharp cone configurations typical of the T5 tunnel at Caltech and investigated second mode synchronization with the slow acoustic spectrum. They investigated the effect of nonlinear disturbances,[33,34] a flared cone geometry,[35] and high-temperature effects,[36] although the Prandtl number and ratio of specific heats were fixed in their real gas model. Overall, Salemi[37] concluded that the synchronization of mode F1 with the slow acoustic spectrum caused the emission of acoustic waves from the boundary layer into the free stream. In 2017, the results of Sescu *et al.*[38] were indicative of the supersonic mode in cold-wall flat plate flow, although the focus of the study was the effect of surface deformations on boundary layer stability. A contemporary study directly focusing on the supersonic mode was performed in 2015 by Bitter and Shepherd,[24] who provided clear evidence through LST of the supersonic mode's existence on a cold-wall flat plate, although they neglected chemical nonequilibrium effects. Bitter and Shepherd also demonstrated the cause of the supersonic mode was the synchronization of mode F1 with the slow acoustic spectrum that occurred on highly-cooled walls. The following year in 2016 Chuvakhov and Fedorov[25] largely confirmed Bitter and Shepherd's[24] findings through perfect gas LST analysis as well as unsteady DNS analysis on a flat plate, although they used different free stream conditions.

Despite the evidence presented by Bitter and Shepherd[24] and Chuvakhov and Fedorov,[25] it is possible that the impact of the highly-cooled wall on the spontaneous radiation of sound may have been overstated because chemical nonequilibrium was not accounted for. Recent theoretical results by Anatoli Tumin in 2017[39] and Edwards and Tumin[40] indicate the spontaneous radiation of sound in flows with $T_w/T_e > 1$. Edwards and Tumin[40] incorporated additional source terms in their mean flow equations accounting for kinetic fluctuations in the flow, but used a perfect gas stability solver. Edwards and Tumin suggested that these kinetic fluctuations may play a role in the creation of the supersonic mode. In addition, in 2018 Knisely and Zhong[19] performed thermochemical nonequilibrium LST and DNS studies using similar hot wall flow conditions on a 5-degree half-angle blunt cone and confirmed the existence of the supersonic mode, although it was quite weak and was due to the interaction of mode S, mode F1, and the slow acoustic continuous spectrum. This phenomenon may be attributed to the real gas effect and may have been overlooked in previous simulations assuming chemical equilibrium. This study performs a more in-depth analysis of the supersonic mode incorporating real gas effects on a blunt cone. The blunt cone is

intended to provide more practical results compared to the flat plate used in previous studies. The goals are to use thermochemical nonequilibrium DNS and LST analyses to: (1) Determine the characteristics of the supersonic mode and under what conditions it exists, and (2) Examine the impact of the supersonic mode on transition to turbulence under realistic flight or experimental conditions.

II. Simulation Conditions

The flow conditions for this study are summarized in Table 1 and are intended to be similar to those used by Edwards and Tumin.[40] The geometry is a 5 degree half-angle axisymmetric blunt cone 1 meter in length with a nose radius of 1 mm. The DNS simulations used 256 points in the wall-normal direction and roughly 5 points per millimeter on the surface of the cone in the streamwise direction. In the azimuthal direction, four points are used. LST simulations interpolated the DNS meanflow onto the LST grid defined by the stretching methods discussed in the following sections.

Table 1. Flow conditions for DNS simulations.

Parameter	Case 1	Case 2
M_∞	10	10
$H_{0,\infty}$	14.78 MJ/kg	14.78 MJ/kg
ρ_∞	1.91 E-2 kg/m^3	1.91 E-2 kg/m^3
p_∞	4 kPa	4 kPa
T_w	1000 K	300 K
T_w/T_∞	1.43	0.43

As will be explained in the following sections, the DNS code used in this study utilizes a shock-fitting method. Thus, the parameters in Table 1 are the free stream conditions upstream of the shock formed over the body.

III. Governing Equations and Gas Model

The governing equations for the DNS and LST codes are those developed by Mortensen and Zhong,[41–46] which are formulated for thermochemical nonequilibrium assuming a two-temperature model. Their formulation is highlighted here for clarity. The rotational mode is assumed to be fully excited with up to eleven non-ionizing species with finite-rate chemistry. Two-temperatures are used to represent translation-rotation energy and vibration energy. There are two species models: an eleven-species model (N_2, O_2, NO, C_3, CO_2, C_2, CO, CN, N, O, C) used for ablation studies and a five-species model (N_2, O_2, NO, N, and O) used to simulate air. The five species model is used here. The Navier-Stokes equations in conservative form consist of five species mass conservation equations, three momentum conservation equations, the total energy equation, and the vibration energy equation. The governing equations in vector form are written as

$$\frac{\partial U}{\partial t} + \frac{\partial F_j}{\partial x_j} + \frac{\partial G_j}{\partial x_j} = W \tag{3}$$

where U is the state vector of conserved quantities, W is the source terms, and F_j and G_j are the inviscid and viscous flux vectors, respectively. For further details of the governing equations and thermochemical model, see the work of Knisely and Zhong[19,47] and Mortensen.[46]

IV. Numerical Methods

A. DNS

The thermochemical nonequilibrium code developed by Mortensen and Zhong[41–46] utilizes a high-order shock-fitting method extended from a perfect gas flow version by Zhong[48] to compute the flow field between the shock and the body. The numerical method is summarized here for clarity. For shock-fitting computations

the shock location is not known *a priori*, so its position is solved along with the flow field. Since the shock position is not stationary, the grid used to compute the flow field is a function of time. The Navier-Stokes equations are transformed into computational space

$$\frac{1}{J}\frac{\partial U}{\partial \tau}+\frac{\partial E'}{\partial \xi}+\frac{\partial F'}{\partial \eta}++\frac{\partial G'}{\partial \zeta}+\frac{\partial E'_v}{\partial \xi}+\frac{\partial F'_v}{\partial \eta}++\frac{\partial G'_v}{\partial \zeta}+U\frac{\partial (1/J)}{\partial \tau}=\frac{W}{J} \tag{4}$$

where J is the Jacobian of the coordinate transformation. Further details of this transformation can be found in Knisely and Zhong[19,47] and Mortensen.[46] A seven point stencil is used to discretize the spatial derivatives

$$\frac{\partial f_i}{\partial x}=\frac{1}{hb_i}\sum_{k=-3}^{3}\alpha_{i+k}f_{i+k}-\frac{\alpha}{6!b_i}h^5\left(\frac{\partial f^6}{\partial^6 x}\right) \tag{5}$$

where h is the step size, $\alpha<0$ is a fifth order upwind explicit scheme, and $\alpha=0$ reduces to a sixth order central scheme. Here the inviscid terms use $\alpha=-6$ which yields a low dissipation fifth order upwinded difference and the viscous terms are discretized using $\alpha=0$. The derivatives in the transverse direction, if required, are treated with Fourier collocation. To compute second derivatives, the first order derivative operator is applied twice. Flux splitting is used for the inviscid flux terms with the eigenvalues of Λ for thermochemical nonequilibrium derived by Liu and Vinokur.[49]

Conditions behind the shock are calculated from Rankine-Hugoniot relations. In the free stream, the flow is assumed to be in thermal equilibrium and the chemical composition of the flow is frozen. The shock is assumed to be infinitely thin which means that the flow has no time to relax as it crosses the shock as relaxation rates are finite. This leads to the chemical composition remaining constant across the shock, as well as the vibration temperature. Since neither process has any time to relax across the shock, the relaxation zone is entirely downstream of the shock. A complete derivation of thermochemical nonequilibrium shock fitting can be found in Prakash et al.[50] A low storage 3rd-order Runge-Kutta method from Williamson[51] is used to advance the solution in time.

B. LST

The linear stability analysis used here is largely based on the LST code developed by Mortensen,[46] however here the assumption of zero wall-normal velocity is relaxed (i.e. $\overline{v}\neq 0$), and freestream boundary conditions incorporating a shock at the computational boundary are used. Mortensen's[46] original LST code has been verified against the work of Hudson,[52] and the modified LST code has been verified by Knisely and Zhong.[47] The LST equations are derived from the governing equations (Eq. 3) where the instantaneous flow is comprised of a mean and fluctuating component $q=\overline{q}+q'$. Here q represents any flow variable such as velocity, density, temperature, etc. The instantaneous flow is then substituted into the governing equations where the steady flow is assumed to satisfy the governing equations and is subtracted out. The mean flow is assumed to be a function of y only i.e. $\overline{q}(x,y,z)=\overline{q}(y)$ and the flow disturbances are assumed to be small i.e. linear. The perturbations are then assumed to be in the form of a normal mode described by $q'=\hat{q}(y)\exp\left[i\left(\alpha x+\beta z-\omega t\right)\right]$, where ω is the circular frequency of the disturbance and α and β are the wavenumbers. For comparison to direct numerical simulation the spatial stability approach is used i.e. α is complex which results in the dispersion relation $\alpha=\Omega(\omega,\beta)$. Substituting in the normal mode form for the perturbation reduces the problem to a coupled set of $ns+5$ ordinary differential equations

$$\left(\mathbf{A}\frac{d^2}{dy^2}+\mathbf{B}\frac{d}{dy}+\mathbf{C}\right)\vec{\phi}=\vec{0}. \tag{6}$$

where $\vec{\phi}=\left[\hat{\rho}_1,\hat{\rho}_2,\ldots,\hat{\rho}_{ns},\hat{u},\hat{v},\hat{w},\hat{T},\hat{T}_V\right]^T$ and $\mathbf{A}$, $\mathbf{B}$ and $\mathbf{C}$ are complex square matrices of size $ns+5$. This is now a boundary value problem where the derivative operators can be discretized and the equations solved numerically.

For hypersonic compressible boundary layers it is important to have high grid resolution near the generalized inflection point.[4] The grid used by Mortensen[46] uses two different functions to cluster points around the inflection point and near the wall. It is called the cosine-exponential grid. In hypersonic flows in which the spontaneous radiation of sound occurs, the cosine-exponential grid may not provide enough grid resolution in the free stream or near the outer shock boundary. The continuous modes oscillate to the computational boundary in many cases. Therefore, it is helpful to use an additional exponential grid stretching function

at the edge of the computational boundary. This second exponential grid stretching function gave better grid spacing in the freestream and clustered points near the edge of the computational boundary,[47] which is desirable when a shock coincides with the boundary. The cosine-double-exponential grid retains the benefits of capturing the sharp increases in eigenfunctions at the wall and at the generalized inflection point, while adding additional resolution in the freestream and near the outer edge boundary.

With the grid defined, Eq. 6 can be transformed into computational space and a numerical representation of the derivatives can be given. The first and second derivative operators in the wall-normal direction are discretized by taking derivatives of Lagrange polynomials in physical space. Here, a five-point stencil is used, resulting in a 4th order method similar to the one used by Malik.[11]

After discretization, nonlinearities exist in α so the global method suggested by Malik[11] is used to compute the eigenvalue spectrum with $\alpha^2 = 0$. This method computes the eigenvalues from a generalized eigenvalue problem $\tilde{A}\vec{\phi} = \alpha\tilde{B}\vec{\phi}$ where the LAPACK[53] subroutine ZGGEV is used here for solution. From the eigenvalue spectrum an initial guess can be obtained for the local method which results in $\overline{A}\vec{\phi} = \overline{B}$ and the eigenvalue is found iteratively without dropping the α^2 terms. The LAPACK subroutine ZGESV is used to solve the local problem. It is also possible to avoid the computationally intensive global method and obtain an initial guess for α from a nearby streamwise location or a DNS simulation assuming the unsteady DNS results are available.

The boundary conditions are required for the freestream and the wall. The wall boundary conditions are linearized non-catalytic conditions for density, no slip, and zero temperature perturbation, although more complex surface boundary conditions can be used for ablation studies.[42,46] In the freestream, the shock boundary conditions developed by Knisely and Zhong[47] were used.

LST gives information about what disturbance frequencies are unstable and the corresponding growth rates of those frequencies, but there is no information on the amplitude of the incoming disturbance. To estimate boundary-layer transition using LST, the e^N transition criterion is used which is defined as

$$e^N = \frac{A(s)}{A_0} = \exp\left[\int_{s_0}^{s} -\alpha_i(s,f)ds\right] \tag{7}$$

where $A(s)$ is the integrated disturbance amplitude, A_0 is the initial disturbance amplitude, s_0 is the location where the disturbance first becomes unstable, and α_i is the spatial amplification rate obtained from LST. The integration is performed for a constant frequency f, and is done numerically using trapezoidal integration. Note that a negative imaginary part of the wave number α results in disturbance growth while a positive value results in disturbance decay. The N-factor is specifically the exponent of e^N. In-flight transition N-factors are commonly understood to be around 10. Malik[21] showed that 9.5 and 11.2 correlated with transition onset for two high Mach number flight tests. In ground test facilities the transition N-factor is usually lower.

V. Steady DNS Results

A. Case 1 Steady DNS Results

Steady DNS translation-rotation temperature, vibration temperature, and mass fraction contours for the nose region of the cone in Case 1 are shown in Fig. 3. The upper half of Fig. 3a is translation-rotation temperature, T, and the lower half is vibration temperature, T_V. Fig. 3a indicates the flow is in thermal nonequilibrium in the nose region. Similarly, the mass fraction of N_2 and O_2 are shown in the upper and lower halves of Fig. 3b, respectively. Fig. 3b indicates the flow is in chemical nonequilibrium. Specifically, O_2 dissociation is the predominant reaction in this flow field, whereas N_2 does not dissociate as severely.

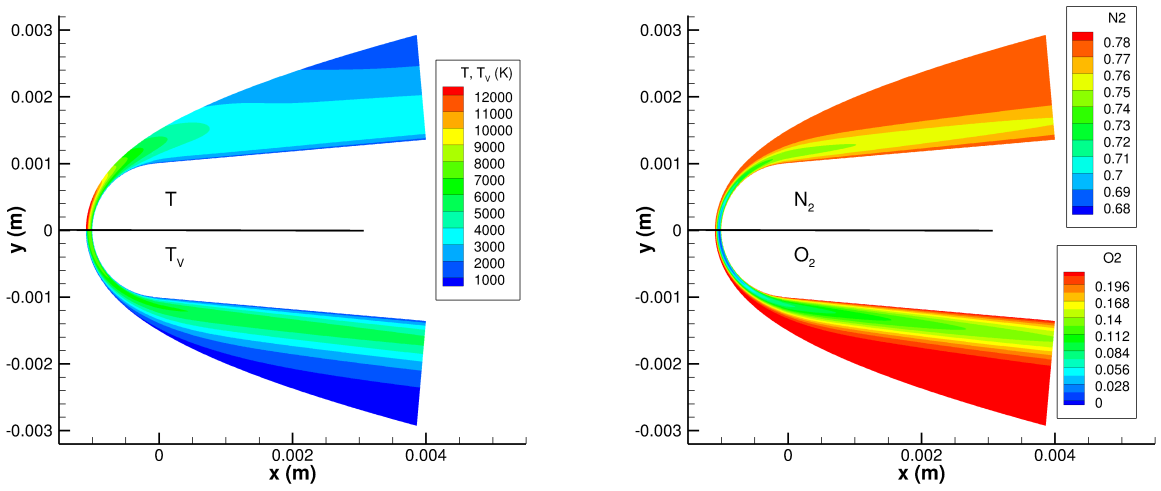

(a) (b)

Figure 3. Case 1 (Hot Wall) Steady flow field contours in nose region. (a) Upper half: T. Lower half: T_V. (b) Mass fraction of N_2 (upper half) and O_2 (lower half).

Farther downstream, the nonequilibrium effects weaken, however there is still significant vibrational and chemical effects. Fig. 4 shows the boundary layer profiles for temperature, vibration temperature, tangential velocity, and species density of N_2 and O_2 at a streamwise distance from the stagnation point of $s = 0.4$ m. Hereafter, y denotes the wall-normal distance. Due to the cold wall, the boundary layer is relatively thin in relation to the flow domain. The mean flow does not reach thermal equilibrium in the free stream, and the species densities of N_2 and O_2 species vary in the free stream, thus demonstrating the necessity of accounting for nonequilibrium effects in these types of flows.

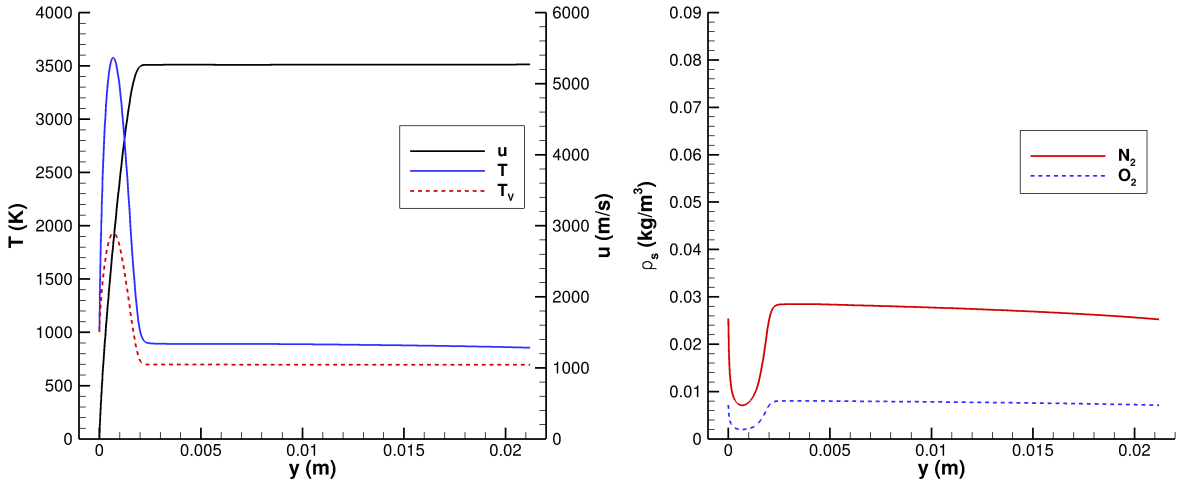

(a) (b)

Figure 4. Case 1 (Hot Wall) mean flow boundary layer profiles at $s = 0.4$ m. (a) u, T, and T_V. (b) Species density ρ_s of N_2 and O_2 species. u denotes the component of velocity tangential to the surface of the cone. y is the wall normal distance.

B. Case 2 Steady DNS Results

The steady DNS translation-rotation temperature, vibration temperature, and mass fraction contours for the nose region of the cone for Case 2 are shown in Fig. 5. Similar nonequilibrium effects occur in Case 2 as in Case 1 because only the wall temperature is varied. Fig. 5a indicates the flow is in thermal nonequilibrium in the nose region, and Fig. 5b indicates the flow is in chemical nonequilibrium. Again, O_2 dissociation is the predominant reaction in this flow field, whereas N_2 does not dissociate as severely.

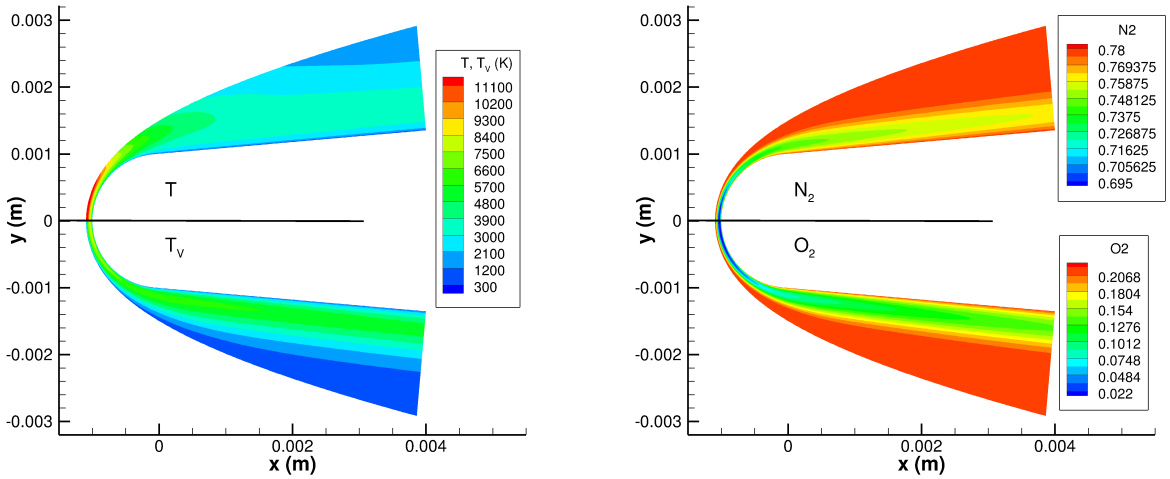

(a) (b)

Figure 5. Case 2 (Cold Wall) Steady flow field contours in nose region. (a) Upper half: T. Lower half: T_V. (b) Mass fraction of N_2 (upper half) and O_2 (lower half).

Farther downstream, the boundary layer profiles (Fig. 6) indicate that Case 4 is in thermal nonequilibrium in the free stream, similar to the previous case. However, the species density of N_2 and O_2 appear to change in magnitude much more than in Case 1, suggesting chemical effects play a larger role near the wall due to the cold wall in Case 2.

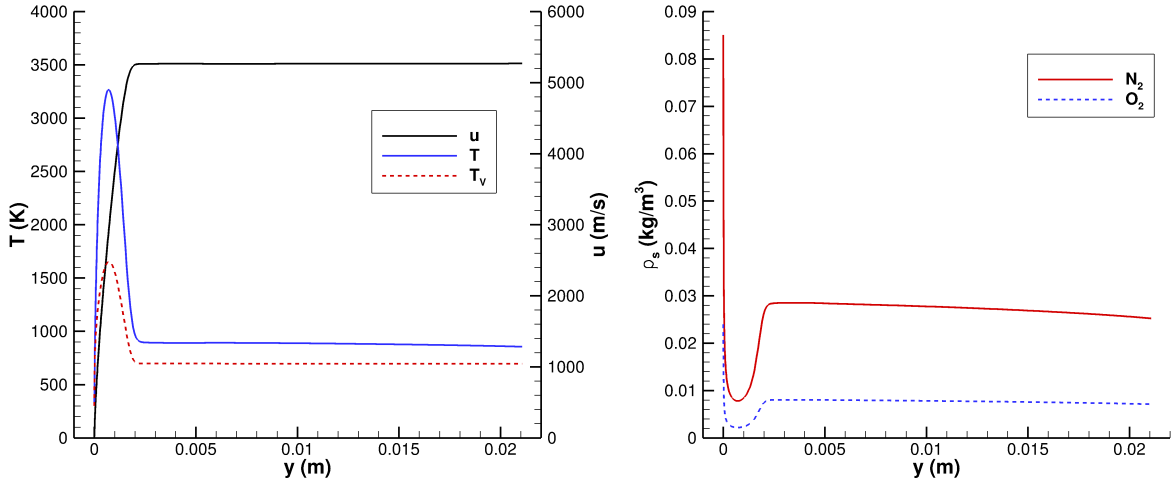

(a) (b)

Figure 6. Case 2 (Cold Wall) mean flow boundary layer profiles at $s = 0.4$ m. (a) u, T, and T_V. (b) Species density ρ_s of N_2 and O_2 species. u denotes the component of velocity tangential to the surface of the cone. y is the wall normal distance.

VI. LST Results

For both Case 1 and Case 2 the freestream values used in nondimensionalizing the LST results were

$$u^*_\infty = 5.303E+03 \text{ m/s}, \quad \rho^*_\infty = 1.991E-02 \text{ kg/m}^3, \quad \mu^*_\infty = 3.320E-05 \text{ kg m/s}.$$

where the nondimensional phase speed is defined as $c_r = \frac{(\omega^*/u^*_\infty)}{\sqrt{\beta^2+\alpha_r^2}}$, where $\omega^* = 2\pi f$ is the dimensional circular frequency and u^*_∞ is the free stream velocity upstream of the shock.

A. Case 1 LST Results

Linear Stability Theory (LST) calculations for Case 1 were performed by Knisely and Zhong;[19] some important results are highlighted here. The phase speed and growth rate curves for $f = 600$ kHz are shown in Figure 7. LST predictions indicated a stable mode F1 and an unstable mode S for Case 1, meaning that there was no supersonic mode expected because the mode S phase speed does not go below the slow acoustic wave speed $c_r = 1 - 1/M_\infty$.

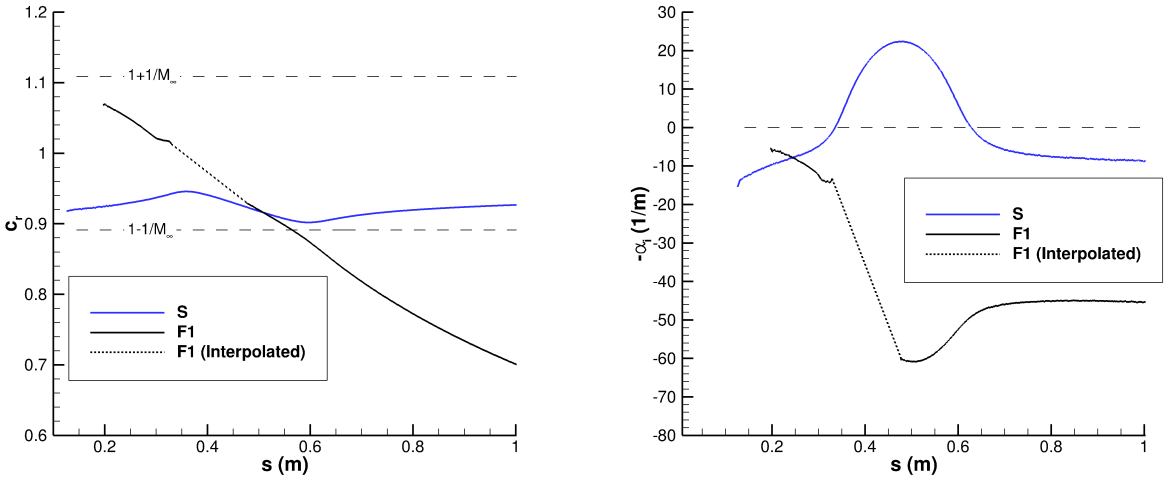

(a) (b)

Figure 7. Case 1 (Hot Wall) LST phase speed and growth rate for Modes F1, F2, and S at $f = 600$ kHz. (a) Phase Speed. (b) Growth Rate.

For a complete picture of the second mode, the stability of mode S for a range of frequencies over the entire length of the cone was computed, resulting in the neutral stability map for mode S (Figure 8a). The neutral stability map indicates the locations and frequencies at which mode S is unstable. The region of instability of the second mode is the area inside the thick black curve. At the lowest frequencies and near the nose of the cone (left-hand side of Figure 8a), the numerical solver is not stable and a physical solution is not obtained. The maximum growth rate occurs at approximately $s = 0.24$ m at a frequency of $f = 840$ kHz. Because mode S is the unstable mode for these conditions, there can exist higher modes that are amplified. Specifically, the third mode amplification is apparent in the upper right corner of Figure 8a. The third mode is amplified after the synchronization of mode F2 with mode S, however this amplification is not sufficient to make the third mode unstable. The second mode is significantly more amplified, and is the predicted cause of transition. To relate the mode S instability to empirical estimates of transition to turbulence, the N-factor curve was calculated, shown in Figure 10b. A maximum N-factor of approximately 6 due to a frequency of $f = 475$ kHz is achieved by the end of the 1 m long cone.

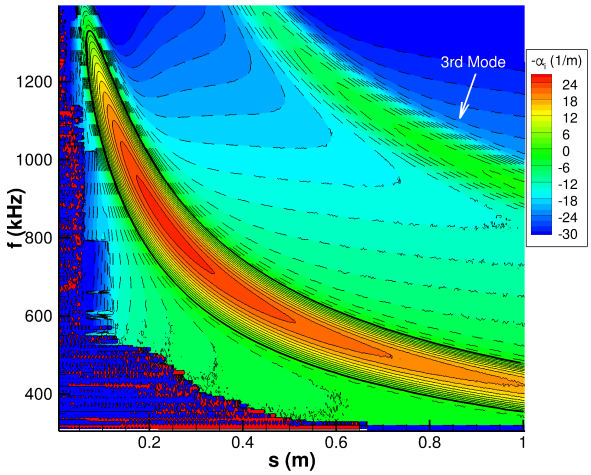

(a) Neutral stability map for mode S. Dashed lines indicate negative growth rates. Thick black line indicates points of neutral stability.

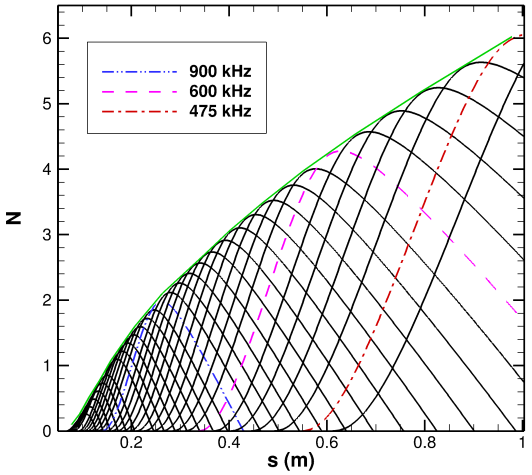

(b) N-factor for unstable second mode frequencies. Frequencies are in increments of $\Delta f = 25$ kHz. The green line is an approximation of the edge of the N-factor curve.

Figure 8. Case 1 (Hot Wall) LST Stability Results. (a) Neutral Contour. (b) N-factor curve.

B. Case 2 LST Results

The phase speed and growth rate curves for Case 2 at $f = 700$ kHz are shown in Figure 9. LST predictions indicate a stable mode F1 and an unstable mode S for Case 2, similar to Case 1. Again, this means that there is no supersonic mode expected because the mode S phase speed does not go below the slow acoustic wave speed $c_r = 1 - 1/M_\infty$.

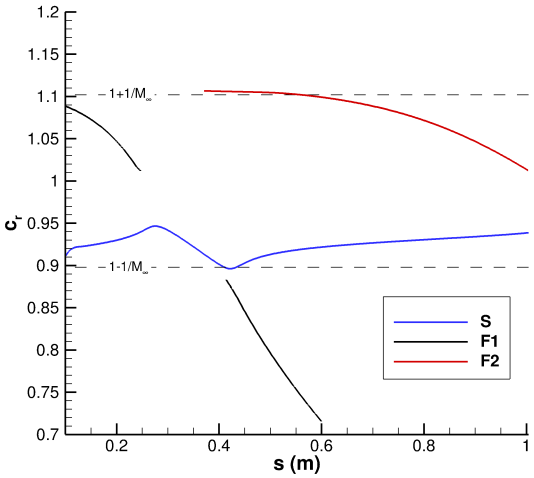

(a)

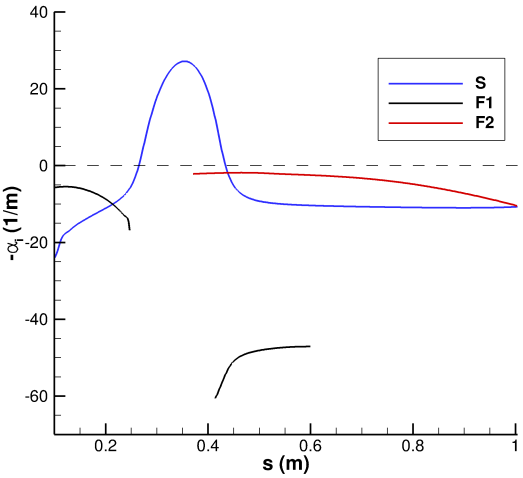

(b)

Figure 9. Case 2 (Cold Wall) LST phase speed and growth rate for Modes F1, F2, and S at $f = 600$ kHz. (a) Phase Speed. (b) Growth Rate.

The neutral stability map for mode S (Figure 10a) was computed for Case 2. Due to the cold wall destabilizing mode S, the third mode is actually unstable in Case 2, while it was stable in Case 1. However, the third mode amplitude is significantly weaker than the second mode, and therefore the second mode is

still the predicted cause of transition. The region of instability of the second and third modes are the areas inside the thick black curves. The maximum growth rate occurs at approximately $s = 0.25$ m at a frequency of $f = 860$ kHz.

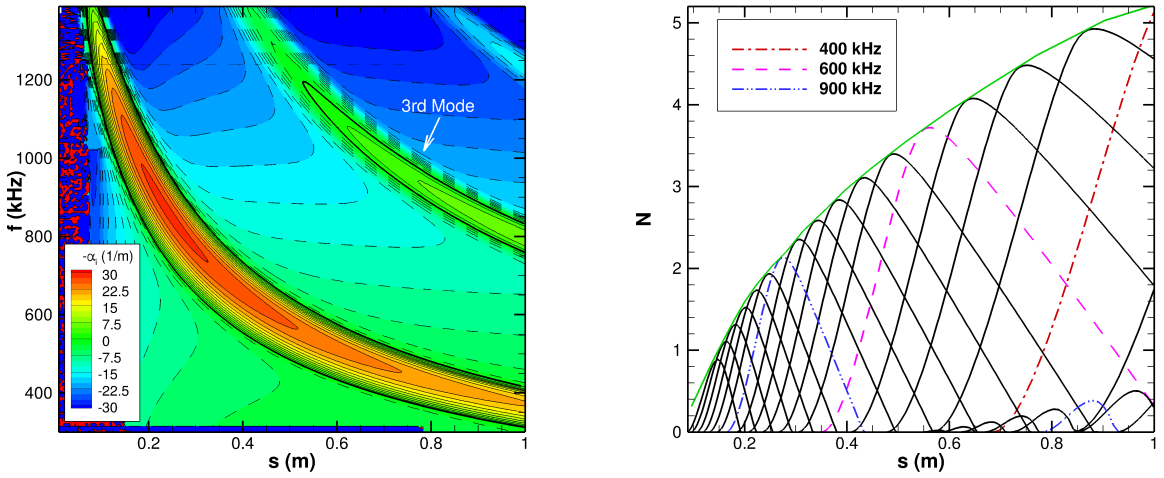

(a) Neutral stability map for mode S. Dashed lines indicate negative growth rates. Thick black line indicates points of neutral stability.

(b) N-factor for unstable second mode frequencies. Frequencies are in increments of $\Delta f = 50$ kHz. The green line is an approximation of the edge of the N-factor curve.

Figure 10. Case 2 (Cold Wall) LST Stability Results. (a) Neutral Contour. (b) N-factor curve.

VII. Unsteady DNS Results

To study stability using DNS, it is required that the meanflow be perturbed in order to study the growth, or decay, of the perturbation. Here, the flow is perturbed with a suction/blowing slot at the cone surface. The equation for the mass flux of the slot is

$$\rho v(x,t)'_w = \epsilon_b (\rho u)_\infty \exp\left\{-\frac{(t-\mu_b)}{2\sigma_b^2}\right\} \sin\left\{\frac{2\pi(x-x_b)}{l_b}\right\} \tag{8}$$

where l_b is the length of the slot, x_b is the center of the slot measured from the leading edge of the cone, ϵ_b scales the function, μ_b shifts the Gaussian component to avoid negative times, and σ_b adjusts the spectral content of the function. Notice the time dependent Gaussian portion of the function. When transformed to frequency space, this yields a continuous range of frequencies with non-zero amplitudes making this particular approach for perturbing the meanflow an effective strategy when studying a wide range of frequencies.

The parameters for the unsteady pulse, given by Equation 8, are summarized in Table 2. The Gaussian pulse and its Fourier transform (Figure 11) show the majority of the frequency content of the pulse is below 1.2 MHz. The same pulse parameters are used for Case 1 and Case 2.

Table 2. Gaussian pulse parameters for unsteady DNS

ϵ_b	μ_b	σ_b	x_b	l_b
$1E-4$	$3E-6$	$3E-7$	$0.1m$	$0.002m$

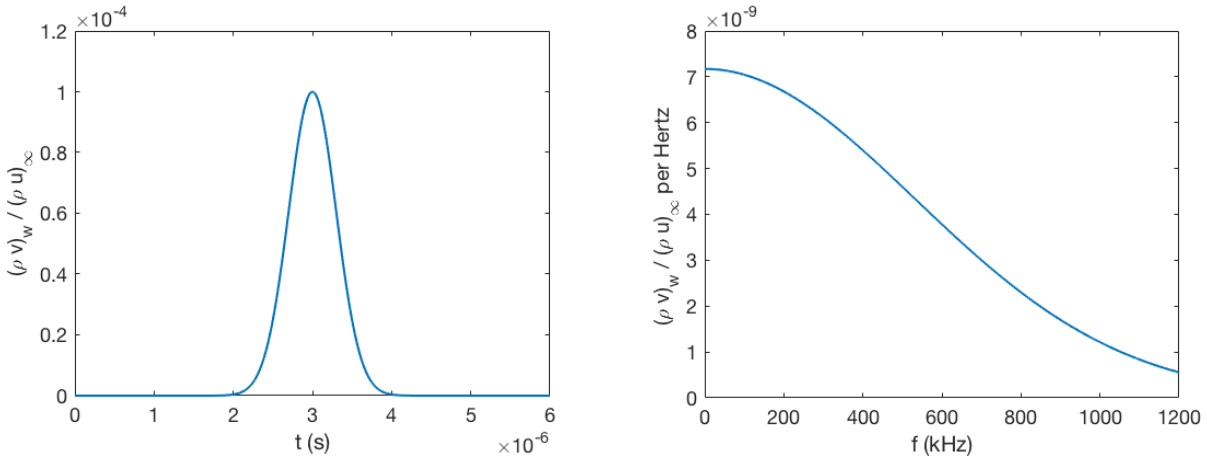

Figure 11. Gaussian pulse for unsteady DNS. (a) Nondimensional mass flux amplitude. (b) Frequency content of pulse.

A. Case 1 Unsteady DNS Results

The evolution of the Gaussian pulse in Case 1 is visualized in Figure 12 using snapshots in time of contours of the pressure perturbation normalized by the local meanflow pressure ($\frac{\Delta p}{p}$). The same value at the surface of the cone is included to more clearly visualize the growth of disturbances. The traditional second mode growth can be seen in Figure 12a between to $x = 0.65$ and $x = 0.7$ m. However, contrary to the LST predictions, the start of the spontaneous radiation of sound appears in Figure 12a for $x < 0.65$ m. When the pulse travels farther downstream, the spontaneous radiation of sound becomes much more apparent, shown in Figure 12b. In particular, the sound radiation is shown very clearly between $x = 0.73$ m and $x = 0.87$ m. Further Fourier decomposition analysis is required to determine whether or not this sound radiation is an artifact of the supersonic mode.

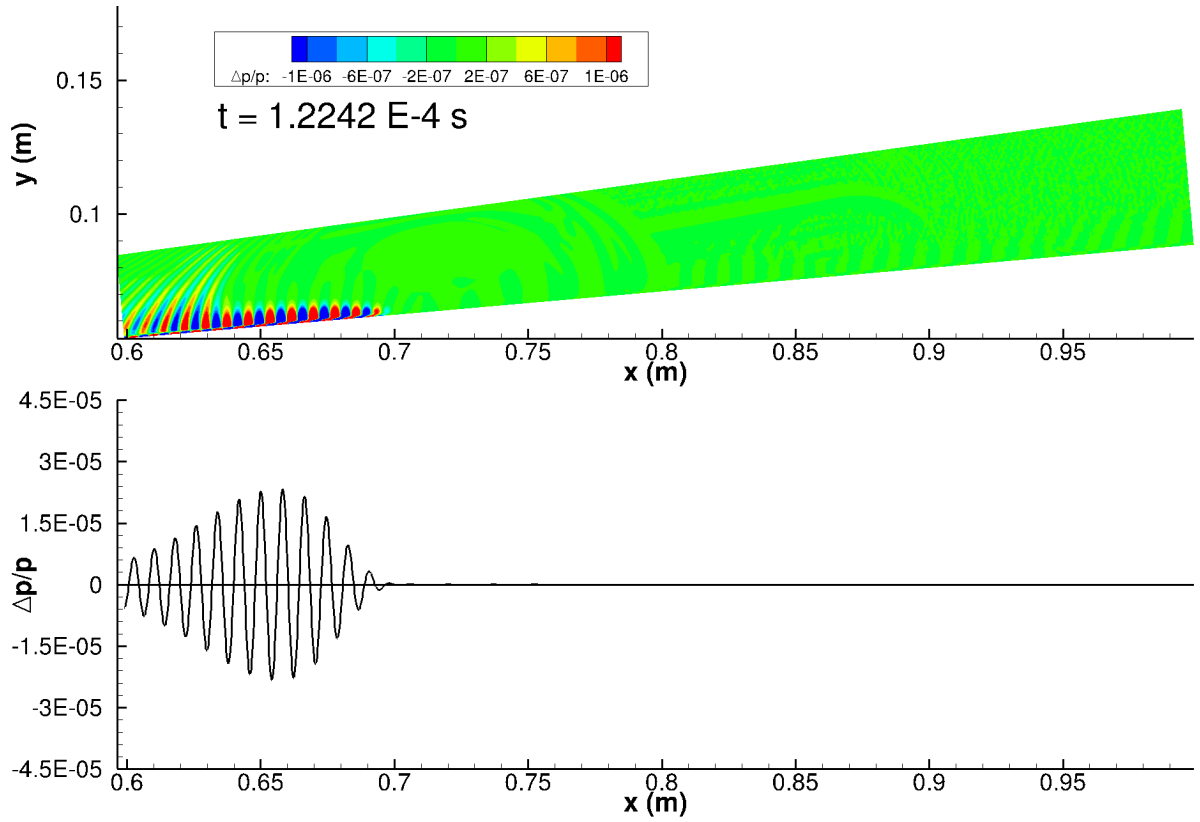

(a)

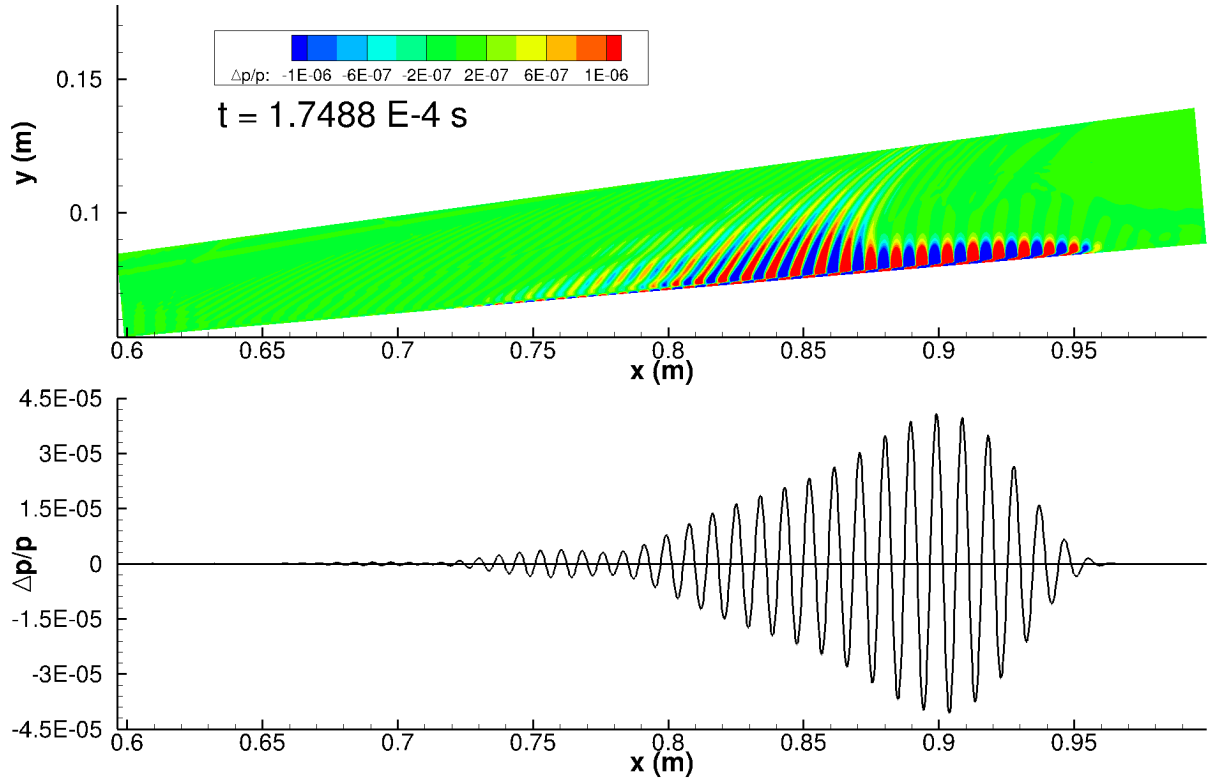

(b)

Figure 12. Case 1 (Hot Wall) snapshots in time of pressure perturbation $\Delta p/p$ contours and surface pressure perturbation from Gaussian pulse. Δt = 5.246 E-5 seconds.

An FFT was performed on the time-history of the surface pressure perturbation at all streamwise locations, resulting in the contour map in Figure 13a. This contour shows the most unstable excited frequencies due to the Gaussian pulse. The neutral stability curve predicted by LST from Figure 8a is overlayed in Figure 13a for comparison. The most amplified frequency from the Gaussian pulse is approximately $f = 475$ kHz and appears most prominently for $s > 0.95$ m. This result agrees remarkably well the the N-factor results from LST. The FFT results follow the LST predictions reasonably closely despite the absence of the radiation of sound in the LST results. It is likely that the amplitude of the supersonic mode is relatively weak in this flow, and the traditional second mode is the dominant instability.

It is useful to compare the FFT results to those obtained by Chuvakhov and Fedorov[25] for a cold-wall flat plate. Although the wall temperature ratio and blowing/suction slot are different than the current study, similar trends are observed for their supersonic mode. The Fourier transform of the unsteady pressure perturbation vs frequency for fixed streamwise locations is shown in Figure 13b. Near the blowing/suction actuator ($s \leq 0.201$ m), the curve shape is similar to a bell curve. However, as the pulse travels downstream, the frequency content shifts and becomes asymmetrical. At each location $s \geq 0.252$ m, there is a dominant peak with at least one smaller amplitude peak occurring at a higher frequency than the dominant frequency. Chuvakhov and Fedorov[25] also obtained similar results for their study, in which they noted that rather than the typical bell-shaped curves, multiple peaks are formed. Chuvakhov and Fedorov[25] observed three peaks at most in their FFT, which largely agrees with the results presented in Figure 13b.

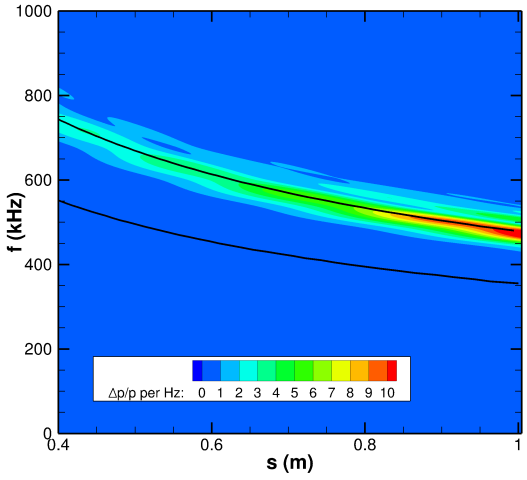

(a) Fourier transform of unsteady surface pressure perturbation time history of Gaussian pulse. The black line is the neutral curve predicted by LST.

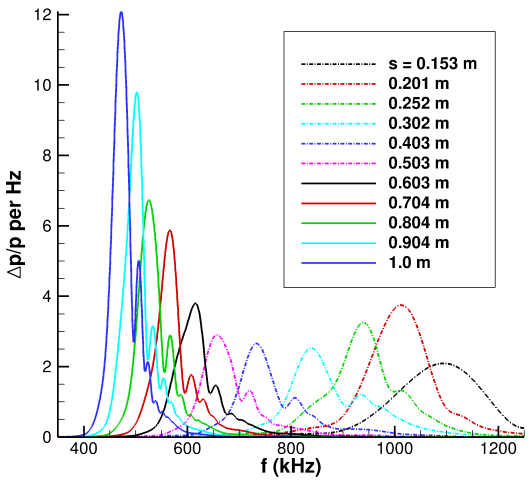

(b) Fourier transform of unsteady surface pressure perturbation time history of Gaussian pulse as a function of frequency for various streamwise locations s.

Figure 13. Case 1 (Hot Wall) FFT of unsteady surface pressure perturbation. (a) Contour map representation. (b) FFT amplitude as a function of f.

It is possible to determine the growth rate and phase speed of an unsteady disturbance in DNS. The Fourier decomposed perturbation variables can be used to reconstruct the perturbation flow field via

$$\phi'(x, y, t) = \Delta\phi(x, y) \exp\left[i(\psi(x, y) - 2\pi f t)\right] \tag{9}$$

where ϕ' is the perturbation of some variable, $\Delta\phi$ is the amplitude of that variable, ψ is the corresponding phase angle, and f represents a single dimensional frequency. The response of the entire flow field for a particular frequency as a result of the unsteady pulse can be given directly by Equation 9, provided FFT data is available for all data points in the flow field.

The FFT of the entire flow field was performed and is shown in Figure 14 for 700 kHz. There is a clear extension of the disturbance outside of the boundary layer, which is typical of the supersonic mode. The onset of the radiation into the free stream for $f = 700$ kHz is near $x = 0.35$ m. For the $f = 700$ kHz frequency, there is a clear amplification in the freestream for $x > 0.7$ m while there is very little amplification

near the wall in this region.

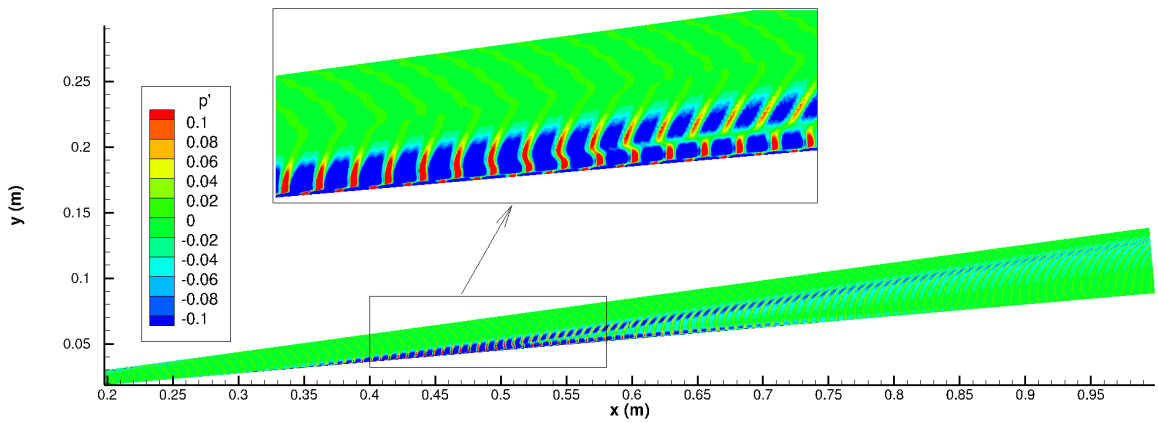

Figure 14. Case 1 (Hot Wall) FFT of unsteady pressure perturbation at all points in the flow field for $f = 700$ kHz.

Multiple boundary layer modes are present simultaneously in DNS, however as one mode becomes dominant, it is possible to derive growth rate, wave number, and phase speed equations for a given frequency f from Equation 9, resulting in

$$-\alpha_i = \frac{1}{\Delta\phi(f)} \frac{d}{ds} \Delta\phi(f) \tag{10}$$

$$\alpha_r = \frac{d}{ds} \psi(f) \tag{11}$$

$$c_r = \frac{2\pi f}{\alpha_r} \tag{12}$$

where s is the streamwise coordinate, $\Delta\phi(f)$ represents a variable amplitude frequency f, and $\psi(f)$ represents the corresponding phase angle at frequency f. Similar to previous researchers,[54] the surface pressure perturbations from DNS are used to compute $-\alpha_i$ and c_r.

The phase speed and growth rate calculated from DNS is compared to the LST predictions for a frequency of $f = 700$ kHz in Figure 15. The DNS matches the LST predictions reasonably well, with a few areas of exception. The DNS and LST mode S results are similar in the region $0.35 < s < 0.4$ m due to mode S being the dominant mode, although the DNS phase speed is slower than predicted by LST, and the DNS growth rate is larger than predicted by LST. Downstream of $s = 0.45$ m, the DNS results oscillate about the LST mode S predictions for both phase speed and growth rate. This oscillatory behavior is the result of multiple modes existing simultaneously in the DNS simulation that are ignored in LST. However, the agreement between DNS and LST is still strong considering the largely different methods used to obtain the results.

This extension of the disturbance into the freestream is typical of the supersonic mode. However, upon closer inspection of the growth rate, phase speed, and eigenfunctions of the DNS results, it is apparent that the dominant mode S is not the cause of the sound radiation. Rather, it is the collective interaction of mode S, mode F1, and the slow acoustic spectrum that causes the supersonic mode in this case.

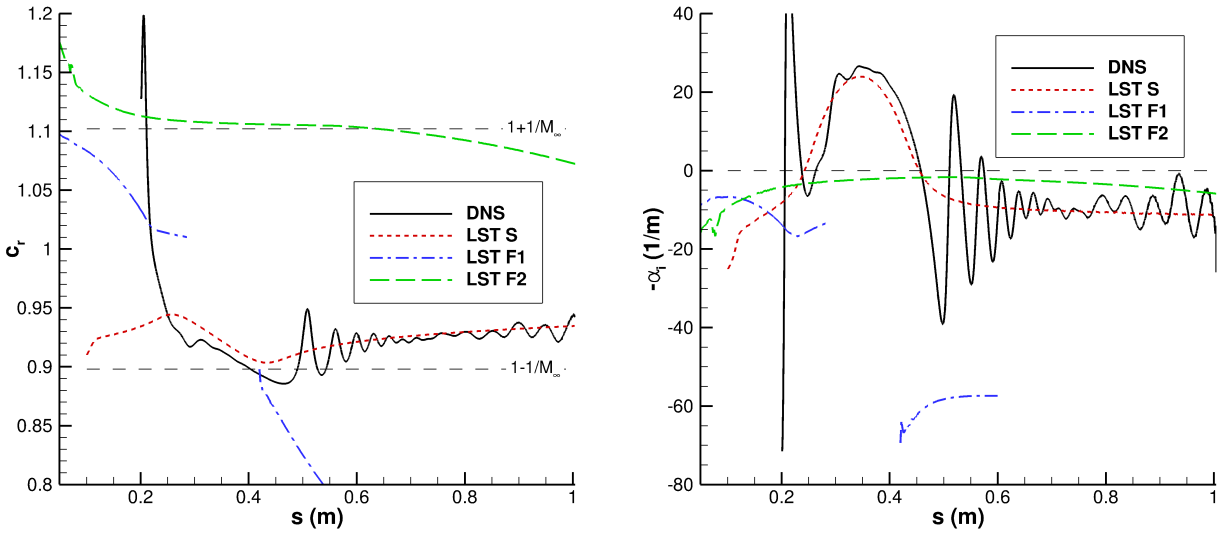

(a) (b)

Figure 15. Case 1 (Hot Wall) comparison of DNS to LST phase speed and growth rate at $f = 700$ kHz. (a) Phase speed, c_r. (b) Growth rate, $-\alpha_i$.

As Knisely and Zhong[19] have noted, there is a modal energy exchange causing a resonant amplification of the stable mode F1 disturbance. This interaction acts as a source term and causes sound to radiate away from the wall. The sound radiation outside of the boundary layer continues to travel downstream and its amplitude becomes slowly damped. Near the wall, however, the resonant interaction quickly ceases, mode F1 is stable, and mode S becomes stable as well, causing the disturbance amplitude to decrease. This scenario would explain the sound radiation in the freestream and the decay of the perturbation at the wall observed in Figure 14. This type of modal interaction is indeed very similar to the creation of the supersonic mode, however it is not predicted by LST because of the assumption that each mode acts independently. In the creation of the supersonic mode, the discrete mode undergoes significant modulation and can be predicted by LST. However, the discrete mode S does not have a supersonic phase speed ($c_r < 1 - 1/M_\infty$) and mode F1 is predicted to be stable by LST. Therefore, because the supersonic mode in this flow is the result of the interaction of modes, it is not expected that the radiation of sound will be apparent in the LST results. To investigate the relative contribution of each mode to the DNS disturbance, a multimode decomposition using methods and tools developed by Gaydos and Tumin[55] and Miselis, Huang, and Zhong[56] must be performed.

B. Case 2 Unsteady DNS Results

Similar to Case 1, the evolution of the Gaussian pulse in Case 2 is visualized in Figure 16 using snapshots in time of contours of $\frac{\Delta p}{p}$ with the same value at the surface of the cone. The traditional second mode growth can be seen in Figure 16a between to $x = 0.71$ and $x = 0.77$ m. However, again contrary to the LST predictions, the start of the spontaneous radiation of sound appears in Figure 16a for $x < 0.71$ m. When the pulse travels farther downstream, the spontaneous radiation of sound becomes much more apparent, shown in Figure 16b. In particular, the sound radiation is shown very clearly between $x = 0.7$ m and $x = 0.95$ m. The magnitude of the surface pressure perturbation in this region of sound radiation is actually larger than the traditional supersonic mode ($x > 0.95$ m), which is not observed in Case 1. Further Fourier decomposition analysis is required to determine whether or not this sound radiation is an artifact of the supersonic mode.

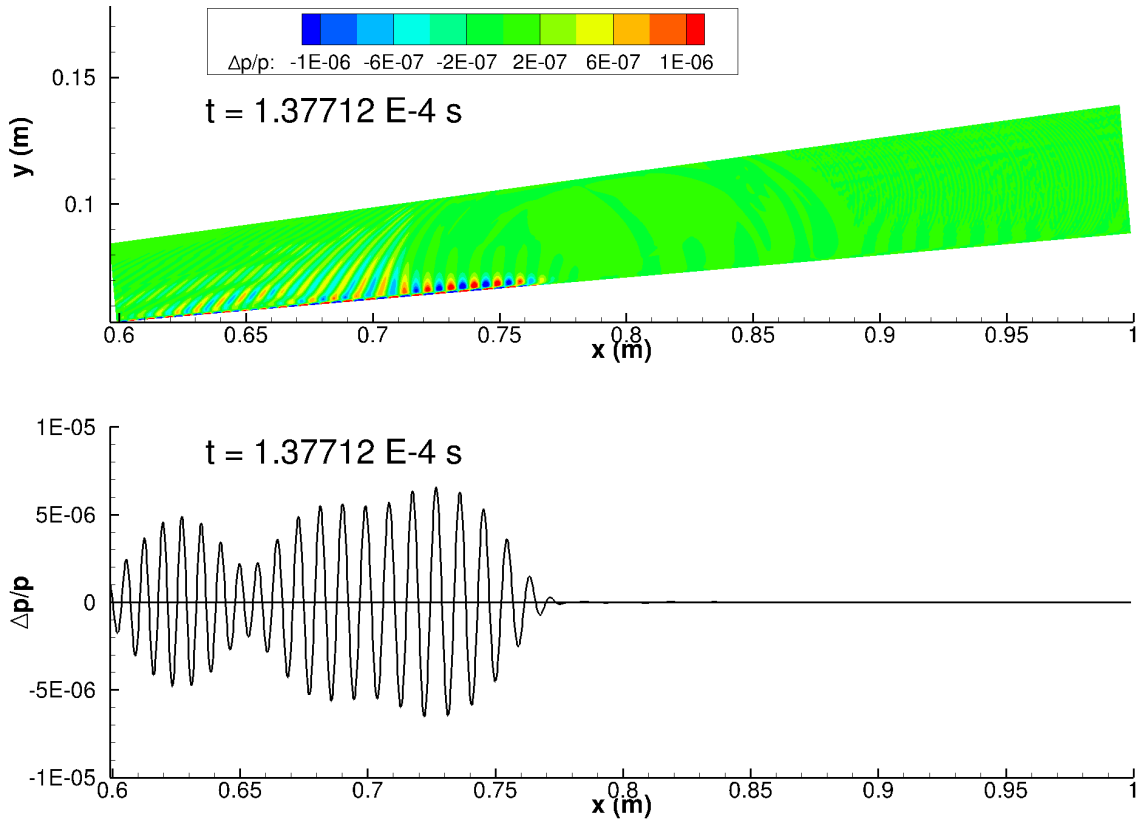

(a)

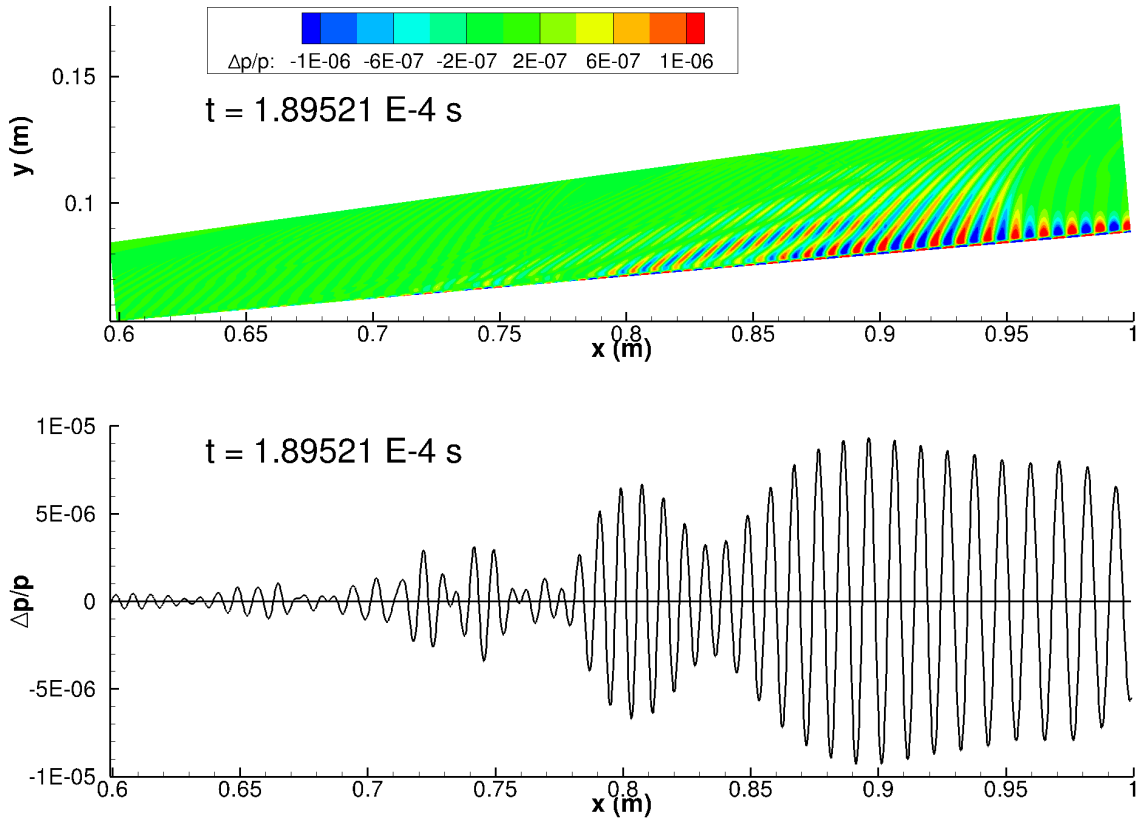

(b)

Figure 16. Case 2 (Cold Wall) snapshots in time of pressure perturbation $\Delta p/p$ contours and surface pressure perturbation from Gaussian pulse. Δt = 5.181 E-5 seconds.

An FFT was performed on the time-history of the surface pressure perturbation at all streamwise locations, resulting in the contour map in Figure 17a. The neutral stability curve predicted by LST from Figure 10a is overlayed in Figure 17a for comparison. The FFT contour generally follows the LST prediction, however the FFT shows streaky behavior with certain frequencies being amplified significantly more than their neighboring frequencies. It is possible that this selective frequency amplification is an artifact of the supersonic mode, as suggested by Chuvakhov and Fedorov.[25] Indeed, when visualizing the FFT data vs. frequency for fixed streamwise locations (Figure 17b), there appear multiple peak frequencies for each fixed streamwise location, just as observed by Chuvakhov and Fedorov.[25]

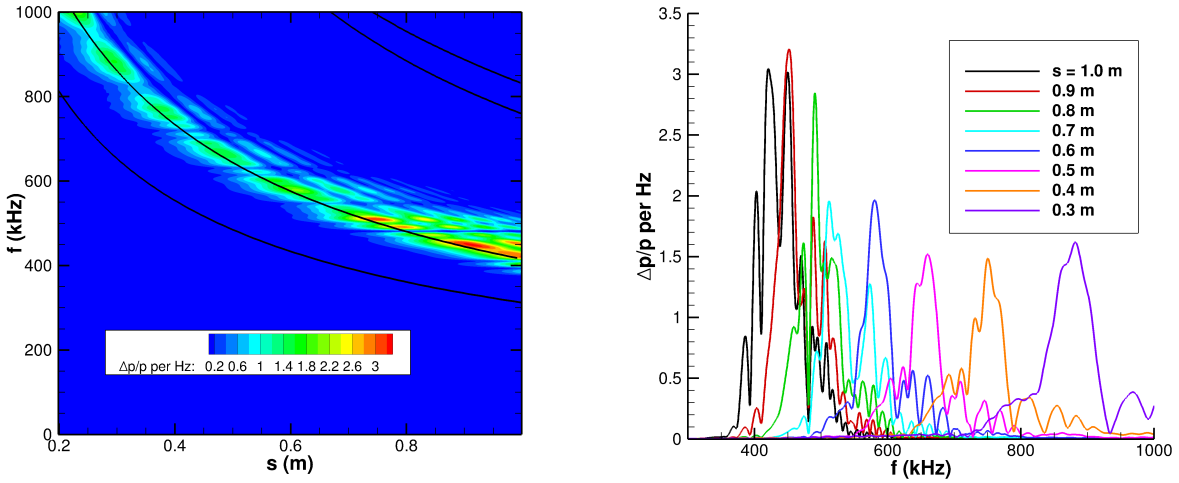

(a) Fourier transform of unsteady surface pressure perturbation time history of Gaussian pulse. The black line is the neutral curve predicted by LST.

(b) Fourier transform of unsteady surface pressure perturbation time history of Gaussian pulse as a function of frequency for various streamwise locations s.

Figure 17. Case 2 (Cold Wall) FFT of unsteady surface pressure perturbation. (a) Contour map representation. (b) FFT amplitude as a function of f.

The FFT of the entire flow field was performed and is shown in Figure 18 for 500 kHz. There is a clear amplification in the freestream for $x > 0.7$ m, while there is still some amplification near the wall in this region, as opposed to the disturbance near the wall decaying in Case 1. This indicates a longer region of sound radiation in Case 2 than Case 1.

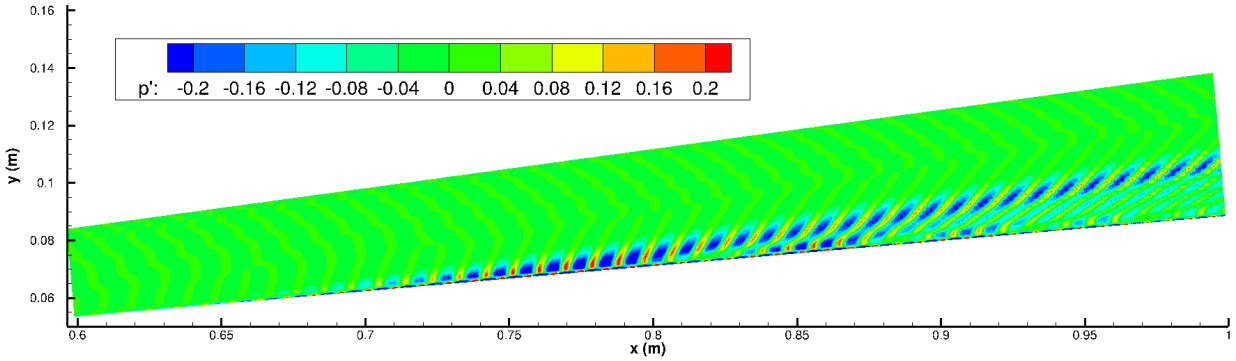

Figure 18. Case 2 (Cold Wall) FFT of unsteady pressure perturbation at all points in the flow field for $f = 500$ kHz.

The phase speed and growth rate calculated from DNS are compared to the LST predictions for a frequency of $f = 500$ kHz in Figure 19. The DNS matches the LST predictions reasonably well for $0.4 < s < 0.75$ m, with significant oscillations in both phase speed and growth rate for $s < 0.4$ m and $s > 0.75$ m. In

the region $0.4 < s < 0.75$ m, the DNS growth rate and phase speed are similar to the LST mode S growth rate and phase speed. However, downstream of $s = 0.75$ m, the DNS phase speed continues to follow the supersonic mode F1 phase speed, rather than the dominant mode S. This type of situation is atypical. There are multiple competing modes in DNS, however there is usually a single dominant mode in this region of instability. In this particular case, the resonant interaction between mode S, mode F1, and the slow acoustic spectrum is strong enough to cause mode F1 to become the dominant instability over mode S. Therefore, the DNS phase speed and growth rate oscillations for $s > 0.75$ m are centered about the supersonic (yet stable according to LST) mode F1. This region of supersonic disturbance propagation causes the sound radiation observed in Figures 16 and 18.

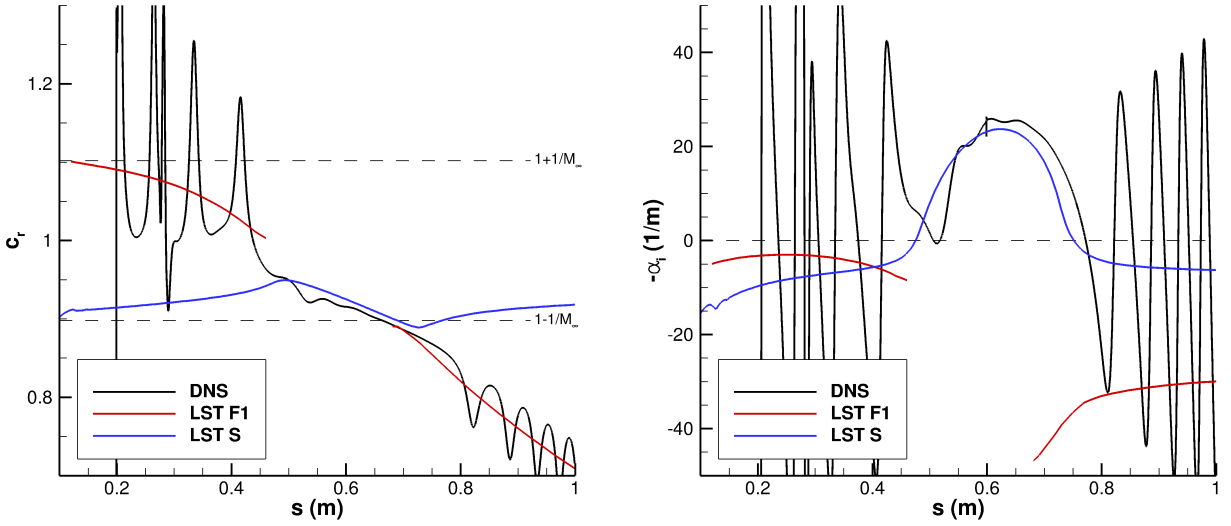

(a) (b)

Figure 19. Case 2 (Cold Wall) comparison of DNS to LST phase speed and growth rate at $f = 500$ kHz. (a) Phase speed, c_r. (b) Growth rate, $-\alpha_i$.

Again, similar to Case 1, there is a modal energy exchange causing a resonant amplification of the stable mode F1 disturbance which acts as a source term and causes sound to radiate away from the wall. However, in Case 2 the amplification of mode F1 is significantly greater than Case 1, causing this brief supersonic mode to actually have higher magnitude than the traditional second mode. The higher magnitude of the supersonic mode is attributed to the colder wall in Case 2. Such a high magnitude resonant amplification has not yet been observed and requires further in depth study. While the conclusion for Case 2 is that a resonant tri-modal interaction between mode F1, mode S, and the slow acoustic spectrum causes the supersonic mode, it is reasonable to suggest this as the mechanism for the creation of the supersonic mode in general.

VIII. Summary and Conclusions

The flow conditions considered here induced significant thermochemical nonequilibrium in the flow downstream of the stagnation point for both the hot and cold wall cases. For both Case 1 (Hot Wall) and Case 2 (Cold Wall), the LST results indicate that mode S is the unstable mode, and therefore no supersonic mode was expected to exist. However, unsteady DNS results of both cases did indicate the presence of sound radiation away from the wall despite LST predicting mode F1 to be stable and mode S to be subsonic. Further FFT analysis indicated that this sound radiation was not due to the dominant mode S directly, but was actually due to the interaction of mode S and mode F1 with the slow acoustic spectrum; a subtle but important distinction. Because mode S is stable and subsonic when this interaction occurs, most LST solvers will not predict the radiative behavior and could affect boundary layer transition prediction. Case 2 exhibited a significantly higher magnitude supersonic mode than Case 1, which was attributed to the colder wall. Surprisingly, the supersonic mode in Case 2 (Cold Wall) actually had a higher magnitude than the traditional second mode and could impact transition unexpectedly if not accounted for. Overall, however,

the results are consistent with previous research[24] showing that a colder wall produces a stronger supersonic mode. In both the hot and cold wall cases, the radiated sound from the wall may have an impact on the stability of the boundary layer, and it is possible the sound radiation acts as an energy sink for the second mode, as suggested by Chuvakhov and Fedorov.[25] Transition prediction tools such as the e^N method should be used with caution when applied to hypersonic boundary layers with the spontaneous radiation of sound.

Acknowledgments

This research was supported by the U.S. Air Force Office of Scientific Research (AFOSR) through the National Defense Science & Engineering Graduate Fellowship (NDSEG) Program. This research was also partially supported by the AFOSR, USAF, under AFOSR Grant #FA9550-15-1-0268, monitored by Dr. Ivett Leyva, and by Office of Naval Research (ONR) Grant #N00014-17-1-2343, monitored by Dr. Knox Millsaps. Primary computational resources were provided by the AFOSR with additional computational resources provided by Extreme Science and Engineering Discovery Environment (XSEDE) through Texas Advanced Computing Center (TACC) and San Diego Supercomputer Center (SDSC) under grant number TG-ASC090076, supported in part by the National Science Foundation. The views and conclusions contained herein are those of the authors and should not be interpreted as necessarily representing the official policies or endorsements, either expressed or implied, of the U.S. Air Force Office of Scientific Research, Office of Naval Research, or the U.S. Government.

References

[1]Reshotko, E., "Hypersonic Stability and Transition," *Hypersonic flows for reentry problems*, Vol. 1, No. A93-42576 17-02, 1991, pp. 18–34.

[2]Zhong, X. and Wang, X., "Direct Numerical Simulation on the Receptivity, Instability, and Transition of Hypersonic Boundary Layers," *Annual Review of Fluid Mechanics*, Vol. 44, 2012, pp. 527–561.

[3]Fedorov, A., "Transition and Stability of High-Speed Boundary Layers," *Annual Review of Fluid Mechanics*, Vol. 43, 2011, pp. 79–95.

[4]Mack, L. M., "Boundary Layer Linear Stability Theory," Tech. rep., AGARD report No. 709, 1984.

[5]Mack, L. M., "Boundary layer stability theory," Tech. Rep. 900-277, JPL Report, 1969.

[6]Demetriades., A., "Hypersonic viscous flow over a slender cone; part iii: Laminar instability and transition." *AIAA 74-535*, 1974.

[7]Zhang, C.-H., Tang, Q., and Lee, C.-B., "Hypersonic boundary-layer transition on a flared cone," *Acta Mechanica Sinica*, Vol. 29, No. 1, 2013, pp. 48–53.

[8]Zhong, X. and Ma, Y., "Boundary-layer receptivity of Mach 7.99 flow over a blunt cone to free-stream acoustic waves," *Journal of Fluid Mechanics*, Vol. 556, 2006, pp. 55–103.

[9]Parsons, N., Zhong, X., Kim, J., and Eldredge, J., "Numerical Study of Hypersonic Receptivity with Thermochemical Non-Equilibrium on a Blunt Cone," *AIAA 2010-4446*, 2010.

[10]Heitmann, D. and Radespiel, R., "Simulation of the interaction of a laser generated shock wave with a hypersonic conical boundary layer," *AIAA 2011-3875*, 2011.

[11]Malik, M. R., "Numerical Methods for Hypersonic Boundary Layer Stability," *Journal of Computational Physics*, Vol. 86, 1990, pp. 376–413.

[12]Stuckert, G. and Reed, H., "Linear Disturbances in Hypersonic, Chemically Reacting Shock Layers," *AIAA Journal*, Vol. 32, No. 7, 1994, pp. 1384–1393.

[13]Hudson, M. L., Chokani, N., and Candler, G., "Linear Stability of Hypersonic Flow in Thermochemical Nonequilibrium," *AIAA Journal*, Vol. 35, No. 6, 1997, pp. 958–964.

[14]Johnson, H. B., Seipp, T. G., and Candler, G., "Numerical study of hypersonic reacting boundary layer transition on cones," *Physics of Fluids*, Vol. 10, No. 10, 1998, pp. 2676–2685.

[15]Johnson, H. B. and Candler, G., "Hypersonic Boundary Layer Stability Analysis Using PSE-Chem," *AIAA 2005-5023*, 2005.

[16]Johnson, H. B. and Candler, G., "Analysis of Laminar-Turbulent Transition in Hypersonic Flight Using PSE-Chem," *AIAA 2006-3057*, 2006.

[17]Mack, L., "Review of Linear Compressible Stability Theory," *Stability of Time Dependent and Spatially Varying Flows*, edited by D. Dwoyer and M. Hussaini, Springer-Verlag, 1985, pp. 164–187.

[18]Mack, L. M., "On the Inviscid Acoustic-Mode Instability of Supersonic Shear Flows Part 1: Two-Dimensional Waves," *Theoretical Computational Fluid Dynamics*, Vol. 2, 1990, pp. 97–123.

[19]Knisely, C. and Zhong, X., "Supersonic Modes in Hot-Wall Hypersonic Boundary Layers with Thermochemical Nonequilibrium Effects," *AIAA 2018-2085*, 2018.

[20]Sherman, M. M. and Nakamura, T., "Flight test measurements of boundary-layer transition on a nonablating 22 deg cone," *Journal of Spacecraft and Rockets*, Vol. 7, No. 2, 1970, pp. 137–142.

[21]Malik, M. R., "Hypersonic flight transition data analysis using parabolized stability equations with chemistry effects," *Journal of Spacecraft and Rockets*, Vol. 40, No. 3, 2003, pp. 332–344.

[22]Lees, L., "The Stability of the Laminar Boundary Layer in a Compressible Fluid," Tech. Rep. 876, NACA, 1947.

[23]Mack, L., "Effect of cooling on boundary-layer stability at Mach number 3," *Instabilities and Turbulence in Engineering Flows*, edited by D. Ashpis, T. Gatski, and R. Hirsch, Springer-Verlag, 1993.

[24]Bitter, N. and Shepherd, J., "Stability of highly cooled hypervelocity boundary layers," *Journal of Fluid Mechanics*, Vol. 778, 2015, pp. 586–620.

[25]Chuvakhov, P. and Fedorov, A., "Spontaneous radiation of sound by instability of a highly cooled hypersonic boundary layer," *8th AIAA Flow Control Conference*, , No. AIAA 2016-4245, 2016.

[26]Chang, C.-L., Vinh, H., and Malik, M., "Hypersonic Boundary-Layer Stability with Chemical Reactions using PSE," *28th AIAA Fluid Dynamics Conference, Snowmass Village, CO, U.S.A.*, 1997.

[27]Fedorov, A., Bres, G., Inkman, M., and Colonius, T., "Instability of hypersonic boundary layer on a wall with resonating micro-cavities," *49th AIAA Aerospace Sciences Meeting*, , No. AIAA 2011-373, 2011.

[28]Wagnild, R., *High Enthalpy Effects on Two Boundary Layer Disturbances in Supersonic and Hypersonic Flow*, Ph.D. thesis, University of Minnesota, 240 Williamson Hall, 231 Pillsbury Drive S.E., Minneapolis, MN 55455, May 2012.

[29]Bres, G., Inkman, M., Colonius, T., and Fedorov, A., "Second-mode attenuation and cancellation by porous coatings in a high-speed boundary layer," *Journal of Fluid Mechanics*, Vol. 726, 2013, pp. 312–337.

[30]Klentzman, J. and Tumin, A., "Stability and receptivity of high speed boundary layers in oxygen," *AIAA 2013-2882*, 2013.

[31]Jewell, J., *Boundary-Layer Transition on a Slender Cone in Hypervelocity Flow with Real Gas Effects*, Ph.D. thesis, California Institute of Technology, 2014.

[32]Fedorov, A., Soudakov, V., and Leyva, I., "Stability analysis of high-speed boundary-layer flow with gas injection," *7th AIAA Theoretical Fluid Mechanics Conference*, , No. AIAA 2014-2498, 2014.

[33]Salemi, L., Fasel, H., Wernz, S., and Marquart, E., "Numerical Investigation of Wave-packets in a Hypersonic High-Enthalpy Boundary-Layer on a 5 Degree Sharp Cone," *7th AIAA Theoretical Fluid Mechanics Conference*, , No. AIAA 2014-2775, 2014.

[34]Salemi, L., Fasel, H., Wernz, S., and Marquart, E., "Numerical Investigation of Nonlinear Wave Packets in a Hypersonic High-Enthalpy Boundary Layer on a 5 Degree Sharp Cone," *45th AIAA Thermophysics Conference*, , No. AIAA 2015-2318, 2015.

[35]Salemi, L. and Fasel, H., "Linearized Navier-Stokes Simulations of the Spatial Stability of a Hypersonic Boundary-Layer on a Flared Cone," *53rd AIAA Aerospace Sciences Meeting*, , No. AIAA 2015-0838, 2015.

[36]Salemi, L., Gross, A., Fasel, H., Wernz, S., and Marquart, E., "Linearized Navier-Stokes Calculations of the Spatial Stability of a Hypersonic Boundary Layer on a 5 °Sharp Cone with High Temperature Effects," *52nd Aerospace Sciences Meeting*, , No. AIAA 2014-0430, 2014.

[37]Salemi, L., *Numerical Investigation of Hypersonic Conical Boundary-Layer Stability Including High-Enthalpy and Three-Dimensional Effects*, Ph.D. thesis, University of Arizona, 2016.

[38]Sescu, A., Sawaya, J., Sassanis, V., and Visbal, M., "Study of the Effect of Two-dimensional Wall Non-uniformities on High-speed Boundary Layers," *AIAA 2017-4511*, 2017.

[39]Tumin, A., Private Communication, 2016.

[40]Edwards, L. and Tumin, A., "Real Gas Effects on Receptivity to Kinetic Fluctuations: I. Mean Flow Effect," *AIAA 2017-0070*, 2017.

[41]Mortensen, C. H. and Zhong, X., "High-Order Shock-Fitting Method for Hypersonic Flow with Graphite Ablation and Boundary Layer Stability," *AIAA 2012-3150*, 2012.

[42]Mortensen, C. H. and Zhong, X., "Numerical Simulation of Graphite Ablation Induced Outgassing Effects on Hypersonic Boundary Layer Receptivity over a Cone Frustum," *AIAA 2013-0522*, 2013.

[43]Mortensen, C. H. and Zhong, X., "Real Gas and Surface Ablation Effects on Hypersonic Boundary Layer Instability over a Blunt Cone," *AIAA 2013-2981*, 2013.

[44]Mortensen, C. H. and Zhong, X., "Simulation of Second-Mode Instability in a Real-Gas Hypersonic Flow with Graphite Ablation," *AIAA Journal*, Vol. 52, No. 8, 2014, pp. 1632–1652.

[45]Mortensen, C. H. and Zhong, X., "Numerical Simulation of Hypersonic Boundary-Layer Instability in a Real Gas with Two-Dimensional Surface Roughness," *AIAA 2015-3077*, 2015.

[46]Mortensen, C. H., *Effects of Thermochemical Nonequilibrium on Hypersonic Boundary-Layer Instability in the Presence of Surface Ablation and Isolated Two-Dimensional Roughness*, Ph.D. thesis, University of California Los Angeles, 2015.

[47]Knisely, C. and Zhong, X., "An Investigation of Sound Radiation by Supersonic Unstable Modes in Hypersonic Boundary Layers," *AIAA 2017-4516*, 2017.

[48]Zhong, X., "High-Order Finite-Difference Schemes for Numerical Simulation of Hypersonic Boundary-Layer Transition," *Journal of Computational Physics*, Vol. 144, No. 2, 1998, pp. 662–709.

[49]Liu, Y. and Vinokur, M., "Nonequilibrium Flow Computations. I. An Analysis of Numerical Formulations of Conservation Laws," *Journal of Computational Physics*, Vol. 83, No. 2, 1989, pp. 373–397.

[50]Prakash, A., Parsons, N., Wang, X., and Zhong, X., "High-order Shock-fitting Methods for Direct Numerical Simulation of Hypersonic Flow with Chemical and Thermal Nonequilibrium," *Journal of Computational Physics*, Vol. 230, No. 23, 2011, pp. 8474–8507.

[51]Williamson, J., "Low-Storage Runge-Kutta Schemes," *Journal of Computational Physics*, Vol. 35, No. 1, 1980, pp. 48–56.

[52]Hudson, M. L., *Linear Stability of Hypersonic Flows in Thermal and Chemical Nonequilibrium*, Ph.D. thesis, North Carolina State University, 1996.

[53]Anderson, E., Bai, Z., Bischof, C., Blackford, S., Demmel, J., garra, J. D., Croz, J. D., Greenbaum, A., Hammarling, S., McKenney, A., and Sorensen., D., *LAPACK Users' Guide*, Society for Industrial and Applied Mathematics, Philadelphia, PA, 3rd ed., 1999.

[54]Ma, Y. and Zhong, X., "Receptivity of a supersonic boundary layer over a flat plate. Part 1. Wave structures and interactions," *Journal of Fluid Mechanics*, Vol. 488, 2003, pp. 31–78.

[55]Gaydos, P. and Tumin, A., "Multimode Decomposition in Compressible Boundary Layers," *AIAA Journal*, Vol. 42, No. 6, 2004, pp. 1115–1121.

[56]Miselis, M., Huang, Y., and Zhong, X., "Modal Analysis of Receptivity Mechanisms for a Freestream Hot-Spot Perturbation on a Blunt Compression-Cone Boundary Layer," *AIAA 2016-3345*, 2016.